



Deposited via The University of Sheffield.

White Rose Research Online URL for this paper:

<https://eprints.whiterose.ac.uk/id/eprint/103261/>

Version: Accepted Version

Article:

Geers, A.J., Morales, H.G., Larrabide, I. et al. (2016) Wall shear stress at the initiation site of cerebral aneurysms. *Biomechanics and Modeling in Mechanobiology*. pp. 1-19. ISSN: 1617-7959

<https://doi.org/10.1007/s10237-016-0804-3>

The final publication is available at Springer via <http://dx.doi.org/10.1007/s10237-016-0804-3>

Reuse

Items deposited in White Rose Research Online are protected by copyright, with all rights reserved unless indicated otherwise. They may be downloaded and/or printed for private study, or other acts as permitted by national copyright laws. The publisher or other rights holders may allow further reproduction and re-use of the full text version. This is indicated by the licence information on the White Rose Research Online record for the item.

Takedown

If you consider content in White Rose Research Online to be in breach of UK law, please notify us by emailing eprints@whiterose.ac.uk including the URL of the record and the reason for the withdrawal request.

Biomechanics and Modeling in Mechanobiology manuscript No.
(will be inserted by the editor)

1 **Wall shear stress at the initiation site of cerebral aneurysms**

2 **A.J. Geers · H.G. Morales · I. Larrabide ·**
3 **C. Butakoff · P. Bijlenga · A.F. Frangi**

4
5 Received: date / Accepted: date

6 **Abstract** Hemodynamics are believed to play an important role in the initiation of
7 cerebral aneurysms. In particular, studies have focused on wall shear stress (WSS),
8 which is a key regulator of vascular biology and pathology. In line with the obser-
9 vation that aneurysms predominantly occur at regions of high WSS, such as bifurca-
10 tion apices or outer walls of vascular bends, correlations have been found between
11 the aneurysm initiation site and high WSS. The aim of our study was to analyze
12 the WSS field at an aneurysm initiation site that was neither a bifurcation apex nor
13 the outer wall of a vascular bend. Ten cases with aneurysms on the A1 segment of
14 the anterior cerebral artery (ACA) were analyzed and compared with ten controls.
15 Aneurysms were virtually removed from the vascular models of the cases to mimic
16 the pre-aneurysm geometry. Computational fluid dynamics (CFD) simulations were
17 created to assess the magnitude, gradient, multidirectionality, and pulsatility of the
18 WSS. To aid the inter-subject comparison of hemodynamic variables, we mapped
19 the branch surfaces onto a two-dimensional parametric space. This approach made it

Preliminary findings from this study were presented at the International Symposium on Biomechanics in Vascular Biology and Cardiovascular Disease, Montreal, QC, Canada, 28–29 April 2014 and at the European Solid Mechanics Conference, Madrid, Spain, 6–10 July 2015.

A.J. Geers
CISTIB, Universitat Pompeu Fabra, Barcelona, Spain
E-mail: ajgeers@gmail.com

H.G. Morales
Medisys – Philips Research Paris, Paris, France

I. Larrabide
PLADEMA-CONICET, UNICEN, Tandil, Argentina

C. Butakoff
PhySense, Universitat Pompeu Fabra, Barcelona, Spain

P. Bijlenga
Hôpitaux Universitaire de Genève et Faculté de médecine de Genève, Geneva, Switzerland

A.F. Frangi
CISTIB, University of Sheffield, Sheffield, UK

possible to view the whole branch at once for qualitative evaluation. It also allowed us to define a patch for quantitative analysis, which was consistent among subjects and encapsulated all aneurysm initiation sites. To test the reproducibility of our results, CFD simulations were repeated with a second independent observer virtually removing the aneurysms and with a 20 % higher flow rate at the inlet. We found that branches harboring aneurysms were characterized by high WSS and high WSS gradients. Among all assessed variables, the aneurysm initiation site most consistently coincided with peaks of temporal variation in the WSS magnitude.

Keywords aneurysm initiation · cerebral aneurysms · computational fluid dynamics · hemodynamics · image-based modeling · flow pulsatility · wall shear stress

1 Introduction

Cerebral aneurysms are localized, pathological dilatations of cerebral arteries. Their rupture causes subarachnoid hemorrhage and is associated with high rates of morbidity and mortality (Hop et al, 1997). Better understanding of the mechanisms underlying aneurysm initiation is crucial for the development of new preventive and therapeutic strategies (Jamous et al, 2005).

While systemic risk factors such as hypertension and connective tissue disorders may weaken the cerebral arteries' ability to maintain homeostasis, hemodynamic stress appear to be a necessary trigger for the pathological remodeling leading to aneurysm formation (Brown et al, 1990; Stehbens, 1989; Nixon et al, 2010; Penn et al, 2011; Dolan et al, 2013; Sadasivan et al, 2013; Meng et al, 2014; Frösen, 2014; Turjman et al, 2014). In vivo measurements of these stresses are limited by the low spatial and temporal resolution of current imaging techniques (Markl et al, 2012) and the rarity of imaging a patient prior to aneurysm formation. Instead, computational fluid dynamics (CFD) techniques have been employed to simulate the hemodynamics in vascular geometries with the aneurysm virtually removed to approximate the pre-aneurysm condition (Mantha et al, 2006; Baek et al, 2009; Ford et al, 2009; Shmogonya et al, 2009; Singh et al, 2010; Castro et al, 2011; Chen et al, 2013; Kono and Terada, 2013; Lauric et al, 2014) and in vascular geometries derived from rare pre-aneurysm images (Doenitz et al, 2010; Kulcsar et al, 2011; Kono and Terada, 2013; Kono et al, 2014). CFD simulations have also been used to complement histological analyses of aneurysm formation in animal models (Meng et al, 2007; Metaxa et al, 2010).

Hemodynamic studies have strongly focused on wall shear stress (WSS), which is a key regulator of vascular biology and pathology (Dolan et al, 2013). In line with the observation that aneurysms predominantly occur at high WSS regions such as bifurcation apices or outer walls of vascular bends (Kondo et al, 1997; Alnaes et al, 2007; Piccinelli et al, 2011; Alfano et al, 2013), many studies have found correlations between the aneurysm initiation site and high WSS (Castro et al, 2011; Singh et al, 2010; Chen et al, 2013), especially in combination with high positive WSS gradients (WSSG) (Meng et al, 2007; Metaxa et al, 2010; Kulcsar et al, 2011; Kono and Terada, 2013; Kono et al, 2014). Other studies have found correlations with low WSS (Mantha et al, 2006; Doenitz et al, 2010), WSS patterns involving both high and low

WSS (Baek et al, 2009; Lauric et al, 2014), or indices describing the oscillatory nature of the WSS and WSSG (Mantha et al, 2006; Ford et al, 2009; Shimogonya et al, 2009; Chen et al, 2013). These apparent inconsistencies among CFD-based studies can be attributed to the small datasets, variety of aneurysm locations, and subjectivity of data analyses, as pointed out by Chen et al. (Chen et al, 2013), but also to missing patient-specific information about boundary conditions and properties of the arterial wall.

The aim of our study was to analyze the WSS field at the aneurysm initiation site. All included aneurysms were from a single location, which was neither a bifurcation apex nor the outer wall of a vascular bend. Vascular geometries with the aneurysm removed were matched to controls that never formed an aneurysm at that particular location but elsewhere. To standardize the data analysis and simplify the comparison of cases, branches of interest were mapped onto the same parametric space. Tests were performed to measure the reproducibility of the computed WSS field with respect to the observer virtually removing the aneurysm and the flow rate imposed at the inlet.

2 Methods

2.1 Case selection

Twenty patients, ten cases and ten controls, were drawn from a large multicenter database created within the EU-funded project @neurIST (Villa-Uriol et al, 2011). The data collection protocol was approved by individual local ethics committees, and written consent was obtained from patients or, where appropriate, next of kin. The cases were all the patients in the database with an aneurysm on the A1 segment of the anterior cerebral artery (ACA). They were selected because of their remarkable consistency in aneurysm location: all aneurysms were just distal to the internal carotid artery (ICA) bifurcation with nine cases directed posteriorly (cases 1 to 9) and one case directed anteriorly (case 10). Moreover, the location was neither a bifurcation apex nor the outer wall of a vascular bend, which – attributed to being high WSS regions – are the most common aneurysm locations (Kondo et al, 1997; Alnaes et al, 2007; Piccinelli et al, 2011; Alfano et al, 2013). The controls were patients with an aneurysm at the middle cerebral artery (MCA) bifurcation, hence predisposed to having aneurysms, that did not form an aneurysm at the studied location on the A1 segment of the ACA. They were selected to match cases by patient age (within 2 years) and aneurysm hemisphere (left or right). No other information was considered during the selection process.

2.2 Vascular modeling

Patient-specific vascular models, represented by triangular surface meshes, were constructed by segmenting three-dimensional rotational angiography (3DRA) images using a geodesic active regions approach (Bogunović et al, 2011). The ophthalmic

102 artery, anterior choroidal artery, and posterior communicating artery branching off
103 the ICA were preserved if successfully segmented. Touching vessels were removed.
104 Models were smoothed using a geometry-preserving smoothing algorithm (Nealen
105 et al, 2006). To ensure consistency in the extent of the vascular models, inlet and
106 outlet branches were clipped at the same location for all cases and controls. Inlet
107 branches were clipped at a manually selected location at the start of the cavernous
108 segment of the ICA and then extruded 10 mm to allow for flow to develop. Outlet
109 branches were automatically clipped 10 mm from their proximal bifurcation; those
110 shorter than 10 mm were first extruded. The ACA had to be extruded only for control
111 6. Figure 1 shows the vascular models of all cases and controls.

112 Aneurysms were virtually removed from the vascular models of the cases to
113 mimic the pre-aneurysm geometry (Figure 1). Triangle removal and hole filling op-
114 erations were iteratively applied to reconstruct the ACA without aneurysm. Subse-
115 quently, the vascular model was smoothed and inlet and outlet branches were clipped
116 as described in the previous paragraph. To assess the reproducibility of the computed
117 WSS field with respect to this manual procedure, two observers independently re-
118 moved the aneurysm for all cases.

119 The automatic selection of outlet locations made use of centerlines and bifurca-
120 tion origins generated with the Vascular Modeling Toolkit (VMTK) (Antiga et al,
121 2008; Piccinelli et al, 2009). Manual mesh editing operations were performed in
122 @neuFuse (B3C, Bologna, Italy) (Villa-Uriol et al, 2011), a software application de-
123 veloped within @neurIST.

124 2.3 Blood flow modeling

125 Unstructured volumetric meshes were created with ICEM CFD 13.0 (ANSYS, Canons-
126 burg, PA, USA) using an octree approach. Meshes were composed of tetrahedral el-
127 ements with a side length of 0.2 mm and three prism layers with a total height of
128 0.07 mm and a side length of 0.1 mm. The total number of elements ranged from 2.3
129 to 6.7 million, the density from 3124 to 4076 elements per mm^3 , depending on the
130 surface-area-to-volume ratio of the computational domain. This mesh resolution was
131 chosen following previously performed mesh dependency tests (Geers et al, 2014).

132 CFD simulations were created with CFX 13.0 (ANSYS), which is a commercial
133 vertex-centered finite volume solver. We used a second-order advection scheme and a
134 second-order backward Euler transient scheme. Solutions converged until the normal-
135 ized residual of the WSS everywhere in the computational domain was $< 5 \times 10^{-4}$.

136 Blood was modeled as an incompressible Newtonian fluid with density $\rho = 1060 \text{ kg/m}^3$
137 and viscosity $\mu = 4 \text{ mPa s}$. Although blood is a non-Newtonian fluid, assuming con-
138 stant viscosity is appropriate for our problem (Morales et al, 2013). Vessel walls were
139 assumed rigid with a no-slip boundary condition. A parabolic velocity profile was im-
140 posed at the inlet.

141 Since patient-specific flow information was unavailable, we estimated the flow
142 rate waveform at the inlet and imposed zero-pressure boundary conditions at all out-
143 lets. The shape of the flow rate waveform was obtained from Ford et al. who aver-
144 aged the waveform shapes of 17 young, normal volunteers (Ford et al, 2005). The

145 time-averaged flow rate, Q , was obtained using the relationship from Cebal et al.:
 146 $Q = 48.21A^{1.84}T^{-1}$ where Q is in ml/s, A is the inlet's cross-sectional area in cm^2 ,
 147 and T is the period of the cardiac cycle in s. This relationship was obtained by fitting
 148 a power-law function through measurements of Q and A of the ICAs and vertebral
 149 arteries of 11 normal volunteers (Cebal et al, 2008). Reynolds numbers at the inlets
 150 ranged from 62 to 441 with an average of 152. To assess the reproducibility of the
 151 computed WSS field with respect to boundary conditions, we repeated the simula-
 152 tions for all cases and controls with a 20 % higher flow rate at the inlet.

153 The cardiac cycle was discretized in 200 uniformly distributed time steps and, to
 154 reduce the effect of initial transients, the second of two simulated cardiac cycles was
 155 analyzed. These settings were chosen following previously performed time step and
 156 cycle dependency tests (Geers et al, 2014).

157 A total of 50 CFD simulations were created: 10 cases and 10 controls under 'nor-
 158 mal' inflow conditions, 10 cases and 10 controls under 'high' inflow conditions, and
 159 10 cases under 'normal' inflow conditions with the aneurysm removed by the second
 160 observer.

161 2.4 Hemodynamic variables

162 As mentioned in the Introduction (Section 1), different aspects of the WSS field are
 163 deemed relevant to the initiation of aneurysms. Specifically, we assessed the magni-
 164 tude, gradient, multidirectionality, and pulsatility of the WSS, according to the defi-
 165 nitions below.

166 Given WSS vector $\tau_w = \tau_w(x, t)$ at surface point x and time t , the time-averaged
 167 WSS magnitude (TAWSS) is defined as

$$\text{TAWSS} = \frac{1}{T} \int_0^T |\tau_w| dt \quad (1)$$

168 where T is the period of the cardiac cycle.

169 For use in the definition of other WSS-related variables, we defined unit vectors
 170 in the direction of and perpendicular to the time-averaged WSS vector, respectively
 171 \hat{p} and \hat{q} , as

$$\hat{p} = \frac{\int_0^T \tau_w dt}{\left| \int_0^T \tau_w dt \right|}, \quad \hat{q} = \hat{p} \times \hat{n} \quad (2)$$

172 where \hat{n} is the surface normal.

173 For the gradient of TAWSS (TAWSSG), we used the definition proposed by Meng
 174 and colleagues (Tremmel et al, 2010; Dolan et al, 2013), which differentiates between
 175 positive and negative gradients with respect to \hat{p} , namely,

$$\text{TAWSSG} = \nabla_S (\text{TAWSS}) \cdot \hat{p} \quad (3)$$

176 where ∇_S is the gradient on the vessel wall surface.

177 Throughout the cardiac cycle, the WSS vector may change direction and not re-
 178 main parallel to \hat{p} . The changing WSS direction is associated with the concept of

179 ‘disturbed’ flow. To quantify the multidirectionality of disturbed flow, we used the
 180 transverse WSS (transWSS), which was recently proposed by Peiffer et al. in the
 181 context of atherosclerosis (Peiffer et al, 2013a). The transWSS is defined as the time-
 182 averaged absolute value of the q -component of the WSS vector, that is,

$$\text{transWSS} = \frac{1}{T} \int_0^T |\tau_w \cdot \hat{q}| dt \quad (4)$$

183 We quantified the temporal variation in the WSS magnitude during the cardiac
 184 cycle by calculating the WSS pulsatility index (WSSPI) (Gosling and King, 1974),
 185 given by

$$\text{WSSPI} = \frac{\max_{t \in [0, T]} \tau_w - \min_{t \in [0, T]} \tau_w}{\text{TAWSS}} \quad (5)$$

186 As the WSS *magnitude* may vary substantially between CFD simulations us-
 187 ing either patient-specific or estimated boundary conditions, caution in interpretation
 188 must be exercised (Karmonik et al, 2010; Marzo et al, 2011; Jansen et al, 2014; Mc-
 189 Gah et al, 2014). We chose to focus on the WSS *distribution* by normalizing TAWSS
 190 by the space-averaged TAWSS on the branch ($\overline{\text{TAWSS}}_B$). For aneurysms, normalized
 191 WSS distributions have been shown to remain relatively unchanged across a range
 192 of physiological boundary conditions (Marzo et al, 2011). TAWSSG and transWSS
 193 were similarly normalized by $\overline{\text{TAWSS}}_B$. Unless stated otherwise, we will report on
 194 normalized values.

195 2.5 Geometric variables

196 Vascular geometry has a major impact on hemodynamics (Geers et al, 2011) and
 197 indeed bifurcations harboring aneurysms tend to more strongly deviate from the op-
 198 timality principle (Baharoglu et al, 2014). To complement the hemodynamic analysis
 199 in our study, we characterized the vascular geometry using the framework presented
 200 by Piccinelli et al. (Piccinelli et al, 2009), which is available as part of VMTK. We
 201 will briefly outline the procedure. Some of the processing steps are illustrated in Fig-
 202 ure 2. For more details, refer to (Piccinelli et al, 2009).

203 Two centerlines were created: one from the inlet to the MCA outlet and another
 204 from the inlet to the ACA outlet. At the ICA bifurcation, the two centerlines diverged
 205 into their respective branches and the corresponding bifurcation origin and plane were
 206 identified. The normal to the bifurcation plane was set to point posteriorly. Center-
 207 lines were split into branches corresponding to the ICA, MCA, and ACA.

208 For each branch, a representative cross sectional area A was defined as the mean
 209 surface area of two cross sections. These two sections were created one and two
 210 maximally inscribed sphere radii away from the bifurcation. The bifurcation’s area
 211 ratio (Ingebrigtsen et al, 2004) was given by

$$\text{area ratio} = \frac{A_{ACA} + A_{MCA}}{A_{ICA}} \quad (6)$$

212 Vectors pointing in the direction of the branches were created and then projected
213 onto the bifurcation plane. The in-plane ICA-ACA and ICA-MCA angles were cal-
214 culated.

215 To quantify the tortuosity of the ACA, we used the definition

$$\text{tortuosity} = \frac{L}{D} - 1 \quad (7)$$

216 where L is the length along the centerline and D is the Euclidean distance between its
217 endpoints.

218 2.6 Branch extraction and parametrization

219 To aid the inter-subject comparison of hemodynamic variables on the surface of the
220 ACA, we used the approach proposed by Antiga et al. (Antiga and Steinman, 2004),
221 which is also available as part of VMTK. Briefly, the vessel wall surface was split into
222 branches corresponding to the previously split centerlines (Figure 2). As branches
223 are topologically equivalent to cylinders, the ACA could be mapped onto a two-
224 dimensional (2D) parametric space with a longitudinal coordinate, u , and a periodic
225 circumferential coordinate, v . Coordinate u ranged from 0 to 10 mm, increasing in the
226 direction of the flow. Coordinate v ranged from $-\pi$ to π rad. The position of $v = 0$
227 was determined by the bifurcation normal parallel transported along the centerline
228 and $v > 0$ was set to correspond to the superior side of the ACA.

229 2.7 Data visualization

230 Contour plots were created to visualize the distribution of hemodynamic variables
231 on the surface of the ACA. Using the 2D parametrization, the branch surface was
232 flattened onto a rectangle such that u and v corresponded to the vertical and horizontal
233 axes of the plots, respectively (Figure 2). This approach made it possible to view
234 the whole branch at once and more easily compare between subjects. Because the
235 circumferential coordinate is periodic, we slightly extended the plot to range from -4
236 to 4 rad, thus maintaining a visual continuity of the variable distributions. To indicate
237 the location of the aneurysm neck, we calculated the distance from the surface with
238 aneurysm to the surface without aneurysm and plotted a contour line at 0.1 mm. The
239 region enclosed by the aneurysm neck will be referred to as ‘aneurysm initiation site’.

240 2.8 Statistical analysis

241 In this study, we assessed the reproducibility of the computed WSS field with respect
242 to the observer virtually removing the aneurysm and to the flow rate imposed at the
243 inlet. Differences between solutions were quantified by calculating the root-mean-
244 square deviation (RMSD) between TAWSS fields, after linearly interpolating them
245 onto a uniformly remeshed branch surface with a nominal node spacing of 0.05 mm.
246 Solutions of observer 2 were projected onto the remeshed branch surface of observer

1. Since normalized TAWSS fields were considered, for which $\overline{\text{TAWSS}}_B = 1$, the RMSD was equal to the coefficient of variation of the RMSD (CVRMSD). CVRMSD will be expressed as a percentage.

Space-averaged values of variables were calculated for quantitative analysis. Besides analyzing the whole branch, we defined a ‘patch’ that encapsulated all aneurysm initiation sites. This patch was bound by $u \in [0, 5]$ and $v \in [-\pi/2, \pi/2]$, see Figure 2. For case 10, with the aneurysm directed anteriorly, and its matching control, the patch was defined at the opposite side of the branch, bound by $u \in [0, 5]$ and $v \in [-\pi, -\pi/2) \cup (\pi/2, \pi]$. Variables were averaged over the branch, patch, and non-patch (branch minus patch).

To test the significance of the differences between regions and between cases and controls, we used the Wilcoxon signed-rank test for paired samples and the Wilcoxon rank-sum test for unpaired samples. Differences were considered statistically significant for $p < 0.05$. The following samples were compared: I. patch vs. non-patch for the cases (paired), II. patch vs. non-patch for the controls (paired), III. patches of the cases vs. patches of the controls (unpaired), and IV. branches of the cases vs. branches of the controls (unpaired).

The Wilcoxon rank-sum test was also used to compare geometric variables between cases and controls. Again, differences were considered statistically significant for $p < 0.05$.

3 Results

3.1 Geometry

As mentioned in Section 2.1, cases in this study were remarkably consistent in location, which is also confirmed by the location of the aneurysm initiation site in Figure 3. For cases 1 to 9, the circumferential coordinate of the center of the initiation site was on average 2° (range: -24 to 13°). For case 10, it was 119° . In other words, most aneurysms were approximately aligned with the transported bifurcation normal.

Table 1 reports on the statistical analysis of geometric variables. Bifurcation angles were very similar among cases and controls. Cross sectional areas of branches tended to be larger for cases, but only for the MCA branch these differences were statistically significant. Area ratios were not significantly different. The tortuosity of ACAs showed a non-significant trend of being larger for cases than for controls.

3.2 Hemodynamics

Figure 3 shows for all cases and controls the non-normalized TAWSS on the ACA. There were large variations in space-averaged TAWSS with values ranging from 1.0 to 11.2 Pa (mean: 3.5 Pa; standard deviation: 2.2 Pa). Figure 4 shows the normalized TAWSS, highlighting the distribution rather than the magnitude. Overall, cases appeared to have a larger spatial variation in TAWSS, covering a wider range of TAWSS

285 values. Close to the apex of the bifurcation and on the superior side of the ACA (Fig-
286 ure 2), TAWSS was relatively high for cases. However, some controls showed sim-
287 ilar patterns, e.g. control 3 and control 5, whereas some cases, e.g. case 6, did not.
288 Aneurysm initiation sites partly overlapped with regions of high TAWSS, yet tended
289 to be near the edge of them. Statistical analysis revealed no significant differences
290 between the patch and the rest of the branch (non-patch) for controls, but did show
291 significant differences between those regions for cases (Table 2). Also, patches of
292 cases experienced significantly higher TAWSS than those of controls. By definition,
293 normalization removed differences in TAWSS between branches.

294 Figure 5 shows the distribution of TAWSSG. Cases' larger spatial variation in
295 TAWSS was reflected by higher positive and negative gradients. Correspondingly,
296 the absolute value of TAWSSG was significantly higher, both for the whole branch
297 and for the patch (Table 2). Although magnitudes varied, distributions were found to
298 be similar for cases and controls: patches experienced significantly higher absolute
299 TAWSSG than the rest of the branch. However, there was no clear correlation between
300 either positive or negative gradients and the aneurysm initiation site.

301 Figure 6 shows the distribution of transWSS. Concentrated regions of high trans-
302 sWSS were observed. WSS vectors changed direction more strongly closer to the ICA
303 bifurcation, which is also reflected by patches having significantly higher transWSS
304 than non-patches (Table 2). On average, transWSS was higher for cases than controls,
305 but only for the whole branch these differences were significant. No clear correlations
306 were found between regions of high transWSS and the aneurysm initiation site.

307 Animations of the WSS field during the cardiac cycle showed that, although the
308 WSS magnitude obviously changed over time, the distribution remained relatively
309 unchanged. Please refer to (Geers et al, 2015a) to view the animations online. This
310 means that at each point on the branch the WSS magnitude over time resembled the
311 shape of a typical flow rate waveform, which motivated our choice for describing
312 the temporal variation with the pulsatility index. Figure 7 shows the distribution of
313 WSSPI. Similar patterns could be observed among cases and controls. Near the bifur-
314 cation, regions of relatively high WSSPI were located on the posterior and anterior
315 side of the ACA and regions of relatively low WSSPI were located on the superior
316 and inferior side (See Figure 2C for a location guide). Further downstream, WSSPI
317 was also relatively low. As a result, we found significant differences between patches
318 and non-patches (Table 2). The main difference between cases and controls was that
319 WSSPI was on average higher for cases, a significant difference for branches but not
320 for patches. Judging from the contour plots, however, we did observe a clear corre-
321 lation between WSSPI peaks and the aneurysm initiation site. Additional statistical
322 analysis confirmed this observation by revealing that WSSPI was significantly higher
323 for just the initiation site than for the whole patch (1.61 vs. 1.52, $p = 0.007$), which
324 was not true for any of the other variables. In other words, among the assessed hemo-
325 dynamic variables, WSSPI most consistently correlated with the aneurysm initiation
326 site.

327 No pattern was found explaining the deviating aneurysm orientation of case 10.
328 Removing the case and its matching control from analysis did not alter the observed
329 trends.

330 3.3 Reproducibility analysis

331 Figure 8 shows the differences in TAWSS distribution between the observers manu-
332 ally removing the aneurysm and between ‘normal’ and ‘high’ flow rates at the inlet.
333 For each comparison, we chose three representative cases or controls, corresponding
334 to minimum, closest-to-mean and maximum CVRMSD. Good reproducibility was
335 found between observers and, although increasing the flow rate by 20 % increased the
336 average TAWSS magnitude by 28 %, the TAWSS distribution remained relatively un-
337 changed. CVRMSD between observers was 6.17 ± 0.07 % (mean \pm standard error),
338 range: 3.57 to 8.05 %. CVRMSD between flow rates was 3.96 ± 0.04 %, range: 2.73
339 to 5.21 %.

340 4 Discussion

341 4.1 Main contributions and findings

342 In summary, the main contributions of this study are: 1. the dataset was drawn from a
343 multicenter database and was composed of cases with aneurysms at a single location,
344 which was not in a known region of high WSS, and a matching set of controls, 2.
345 objective comparison of variable distributions was made possible by automatic ex-
346 traction and parametrization of the branch, 3. to our knowledge, this is the first study
347 to evaluate the transWSS and WSSPI in the context of aneurysm initiation; and 4.
348 tests were performed to assess the reproducibility of the computed WSS field with
349 respect to the observer virtually removing the aneurysm and the flow rate imposed at
350 the inlet.

351 The main findings of this study are: 1. aneurysms form on branches with large
352 spatial variations in TAWSS, as also reflected by the presence of high TAWSSG gra-
353 dients; 2. aneurysms form on branches with large temporal variations in WSS direc-
354 tion (i.e. transWSS); 3. aneurysms form at regions of high TAWSS; and 4. aneurysms
355 form at focal regions with large temporal variations in WSS magnitude (i.e. WSSPI).

356 4.2 Aneurysm location

357 The majority of aneurysms are found at the apex of bifurcations or the outer wall of
358 vascular bends, which has long established the importance of hemodynamic stress in
359 the initiation of cerebral aneurysms (Kayembe et al, 1984; Stehbens, 1989; Gonzalez
360 et al, 1992; Kondo et al, 1997; Foutarakis et al, 1999). At the bifurcation apex, blood
361 impinges the wall and rapidly accelerates and then decelerates as it diverts into the
362 branches. The associated WSS is low at the impingement region and high further
363 downstream, with, along the branch, first high positive and then high negative gra-
364 dients (Dolan et al, 2013). By complementing animal studies with CFD simulations,
365 Meng and colleagues have gathered evidence indicating that the combination of high
366 WSS and positive WSSG triggers the pathological remodeling leading to aneurysm
367 formation (Meng et al, 2007; Metaxa et al, 2010; Dolan et al, 2013). Other CFD stud-
368 ies, using pre-aneurysm images, have corroborated this finding (Kulcsar et al, 2011;

369 [Kono and Terada, 2013](#); [Kono et al, 2014](#)). With respect to the rest of the branch and
370 the controls, we also found aneurysms to form in regions of relatively high WSS and
371 WSSG. However, although regions of positive WSSG were found close to the bifur-
372 cation apex, aneurysms were located further downstream in regions of mixed positive
373 and negative WSSG.

374 Aneurysms also occur at locations with lesser-known hemodynamic conditions.
375 Studying these locations can provide great insight into the hemodynamic mecha-
376 nisms underlying aneurysm initiation. For instance, finding high WSS and WSSG in
377 regions that are not commonly dominated by those WSS characteristics, which can
378 be confirmed with controls, would provide stronger evidence in support of their role
379 in aneurysm initiation. Recently, [Lauric et al.](#) reported on a study of 10 aneurysms
380 located at the inner wall of the carotid siphon and 25 control ICAs ([Lauric et al,](#)
381 [2014](#)). The location was of particular interest as little was known about the hemo-
382 dynamic conditions, except that the WSS was expected to be low. They found that
383 aneurysms had formed in regions of low WSS flanked by peaks of high WSS and
384 WSSG; WSS peaks correlated with the aneurysm necks; and controls were charac-
385 terized by low, almost constant, WSS and WSSG. Similarly, in our study, comparing
386 ACAs harboring aneurysms to ACAs that never formed an aneurysm allowed us to
387 differentiate between hemodynamic stress patterns common to ACAs and those spe-
388 cific to aneurysm formation.

389 4.3 Temporal variation in WSS direction

390 Apart from their magnitudes, research has also focused on the oscillatory nature of
391 the WSS and WSSG vectors. The most commonly used variable in this regard is the
392 oscillatory shear index (OSI), which was introduced in the context of atherosclerosis
393 ([Ku et al, 1985](#)) but later also used to study aneurysm initiation ([Shimogonya et al,](#)
394 [2009](#); [Singh et al, 2010](#); [Kono et al, 2014](#)) and rupture ([Xiang et al, 2011](#); [Miura et al,](#)
395 [2013](#)). Two other variables were introduced specifically to study aneurysm initiation:
396 the (potential) aneurysm formation indicator (AFI) ([Mantha et al, 2006](#)) and the gra-
397 dient oscillatory number (GON) ([Shimogonya et al, 2009](#)). Variable definitions and
398 results for these variables are presented in the appendix (Section 6)

399 [Peiffer et al.](#) recently proposed the transWSS and showed that it captures different
400 flow features than OSI ([Peiffer et al, 2013a](#)). Preliminary results indicated strong
401 correlations with atherosclerotic lesion. Other than OSI and AFI, which give more
402 weight to flow reversal, transWSS focuses solely on the multidirectional (vs. uniaxial)
403 nature of disturbed flow. Given these unique properties, we considered it a relevant
404 new variable to assess in the context of aneurysm initiation.

405 For both cases and controls, regions of high transWSS were concentrated, sug-
406 gesting that flow disturbances remained in the same location throughout the cardiac
407 cycle. As expected, flow was more disturbed closer to the ICA bifurcation, leading to
408 higher transWSS values in that region. Averaged over the whole, cases were found to
409 have significantly higher transWSS values, but there were no clear correlations with
410 the aneurysm initiation site.

411 4.4 Temporal variation in WSS magnitude

412 Among the assessed hemodynamic variables, WSSPI most consistently coincided
413 with the aneurysm initiation site. The variable was introduced as a simple metric
414 to quantify the temporal variation of the WSS magnitude without using noise-prone
415 temporal gradients (Lee et al, 2009). Besides the spatial variation in the WSS mag-
416 nitude, related to the WSSG, and the temporal variation in the WSS direction, our
417 results suggest that the temporal variation in the WSS magnitude is also an important
418 factor to consider when investigating the role of hemodynamic stress in aneurysm ini-
419 tiation. This is in line with the observation that endothelial cells respond differently
420 to temporal vs. spatial variations in WSS (White et al, 2001, 2005) and to different
421 types of pulsatile flow (Helmlinger et al, 1991; Himburg et al, 2007; Feaver et al,
422 2013).

423 4.5 Limitations and future directions

424 Aneurysms were virtually removed to approximate the pre-aneurysm vascular geom-
425 etry. This approach has two main limitations. First, manual removal of aneurysms
426 is observer-dependent. We addressed this by repeating the analysis with a second
427 observer and found good agreement (Figure 8). Other studies employed automatic
428 removal methods (Ford et al, 2009; Shimogonya et al, 2009; Chen et al, 2013), but
429 these preserve less of the vascular geometry and still rely on manually set parameters.
430 Second, aneurysm removal does not account for possible changes in parent vessel
431 geometry due to interaction with the perianeurysmal environment during aneurysm
432 growth (Sforza et al, 2012). Since ICA bifurcations are not near bone structures, sub-
433 stantial changes were unlikely to have occurred. However, prospective studies are
434 needed for confirmation.

435 Discrepancies between estimated and patient-specific flow rate waveforms at the
436 inlet have been shown to strongly affect the WSS magnitude (Karmonik et al, 2010;
437 Marzo et al, 2011; Jansen et al, 2014; McGah et al, 2014), but not the WSS distri-
438 bution (Marzo et al, 2011). Therefore, we focused on the distribution by normalizing
439 appropriate variables by the average WSS on the branch. We also repeated the anal-
440 ysis with a 20 % higher inflow rate to confirm that the WSS distribution remained
441 relatively unchanged. The influence of the waveform shape on the WSSPI should be
442 investigated. Regarding the outlets, despite the simplification of zero-pressure bound-
443 ary conditions, the resulting ACA:MCA flow split of 34:66 closely matched the in
444 vivo measurements (36:64) reported in (Zhao et al, 2007). Although much can be
445 learned from WSS distributions, we wish to stress that CFD studies scrutinizing the
446 role of hemodynamics in aneurysm initiation and rupture would greatly benefit from
447 patient-specific boundary conditions. Ideally, a range of possible boundary condi-
448 tions, covering all the patient's levels of exercise, should be considered to obtain a
449 complete picture of the shear stresses exerted on the arterial wall.

450 Pathogenesis of cerebral aneurysms involves the interplay between mechanical
451 stimuli, vascular biology, and vascular geometry (Meng et al, 2014). Therefore, aneurysm
452 initiation is likely caused by a combination of biochemical and biomechanical fac-

453 tors ([Sadasivan et al, 2013](#)). Although hemodynamic stresses appear to be important,
454 their effect on the vascular biology, i.e. the mechanobiology, should also be modeled
455 to gain a deeper understanding of the underlying mechanisms ([Humphrey and Taylor,](#)
456 [2008](#); [Watton et al, 2009, 2010](#)). Moreover, among hemodynamic stresses, not only
457 the WSS but also pressure-induced tensile stresses are known regulators of vascular
458 biology and should be analyzed ([Meng et al, 2014](#)).

459 5 Conclusions

460 The aim of this study was to analyze the WSS field at the aneurysm initiation site.
461 Ten cases with aneurysms at a single location were analyzed and compared with
462 ten controls. We found that the general region in which aneurysms had formed was
463 characterized by high TAWSS and high TAWSSG. The aneurysm initiation site partly
464 overlapped with regions of high TAWSS and, among all assessed variables, most
465 consistently coincided with peaks of WSSPI.

466 6 Open data

467 To promote the future use of the dataset, surface meshes of all cases (with and without
468 aneurysm) and controls have been made available online at ([Geers et al, 2015b](#)).

469 Conflict of interest

470 None.

471 **Acknowledgements** Financial support for this work was provided by the European Commission through
472 the @neurIST project (FP6-IST-027703). The authors are very grateful to all collaborators within the
473 @neurIST project. In particular, we would like to thank the following institutes for directly contributing
474 to the construction of the @neurIST database (in alphabetical order): Advanced Simulation & Design
475 GmbH, Rostock, Germany (C. Bludszweit-Philipp); ANSYS Europe Ltd, Abingdon, UK (I. Jones, J. Pen-
476 rose); BioComputing Competence Centre, Super Computing Solution s.r.l., Bologna, Italy (A. Chiarini,
477 M. Viceconti); Hospital Clínic i Provincial de Barcelona, Barcelona, Spain (J. Blasco, J. Macho); Hos-
478 pital General de Catalunya, Sant Cugat del Vallès, Spain (T. Sola, E. Vivas); Hôpitaux Universitaires de
479 Genève, Geneva, Switzerland (P. Bijlenga, M. Jägersberg, K.O. Lovblad, A. Marcos-Gonzalez, V. Mendes-
480 Pereira, A.P. Narata, A. Rogers, D.A. Rüfenacht, K. Schaller, B. Schatlo, P. Teta); Royal Hallamshire
481 Hospital, Sheffield, UK (S. Coley, P. Lawford, U. Patel, P. Singh, A. Waterworth); Universitat Pompeu
482 Fabra, Barcelona, Spain (M.L. Aguilar, H. Bogunovic, G. Engelbrecht, A.F. Frangi, A.J. Geers, M. Kim,
483 I. Larrabide, H.G. Morales, C. Valencia-Muñoz, M.C. Villa-Uriol); University of Sheffield, Sheffield, UK
484 (D.R. Hose, R. Lycett, A. Marzo).

485 Appendix: Additional hemodynamic variables

486 This appendix presents variable definitions and results for three additional hemody-
487 namic variables describing the oscillatory nature of the WSS and WSSG vectors.

488 The oscillatory shear index (OSI) was introduced by Ku et al. (Ku et al, 1985) and
489 later redefined by He and Ku (He and Ku, 1996). It describes the oscillatory nature
490 of the WSS vector, τ_w , during the cardiac cycle and has been used extensively in the
491 context of atherosclerosis (Peiffer et al, 2013b) and aneurysm initiation (Singh et al,
492 2010; Shimogonya et al, 2009; Kono et al, 2014). It is given by

$$\text{OSI} = \frac{1}{2} \left(1 - \frac{\left| \int_0^T \tau_w dt \right|}{\int_0^T |\tau_w| dt} \right), \quad \text{OSI} \in \left[0, \frac{1}{2} \right] \quad (8)$$

493 where t is time and T is the cardiac period.

494 The (potential) aneurysm formation indicator (AFI) was proposed by Mantha et
495 al. (Mantha et al, 2006) to identify flow stagnation zones, which in their study of
496 three sidewall aneurysms coincided with the aneurysm initiation site. It measures the
497 cosine of angle θ between the instantaneous WSS vector and the time-averaged WSS
498 vector, that is,

$$\text{AFI} = \cos \theta = \frac{\tau_w}{|\tau_w|} \cdot \hat{p}, \quad \text{AFI} \in [-1, 1] \quad (9)$$

499 AFI was obtained at time point H1 of Ford et al.'s flow rate waveform (Ford et al,
500 2005), corresponding to midsystolic deceleration during which flow is least stable
501 (Fung, 1997, p. 137).

502 The gradient oscillatory number (GON) was proposed by Shimogonya et al. (Shi-
503 mogonya et al, 2009) to quantify the degree of oscillating tension/compression forces
504 at the aneurysm initiation site. It is given by

$$\text{GON} = 1 - \frac{\left| \int_0^T G dt \right|}{\int_0^T |G| dt}, \quad \text{GON} \in [0, 1] \quad (10)$$

505 where

$$G = \begin{pmatrix} \nabla_S (\tau_w \cdot \hat{p}) \cdot \hat{p} \\ \nabla_S (\tau_w \cdot \hat{q}) \cdot \hat{q} \end{pmatrix} \quad (11)$$

506 Contour plots of the three variables are in Figures 9 (OSI), 10 (AFI), and 11
507 (GON).

508 We found strong correlations between variables, implying that they capture the
509 same flow features: AFI correlated with OSI, GON correlated with absolute TAWSSG.
510 This is in accordance with previous studies (Lee et al, 2009; Peiffer et al, 2013a). The
511 distribution of GON was very noisy, which can largely be attributed to it being the
512 temporal variation in the second-order derivative of the velocity (Chen et al, 2013).
513 No clear correlations were found between the variable distributions and the aneurysm
514 initiation site.

References

- 515 **References**
- 516 Alfano JM, Kolega J, Natarajan SK, Xiang J, Paluch RA, Levy EI, Siddiqui AH,
517 Meng H (2013) Intracranial aneurysms occur more frequently at bifurcation sites
518 that typically experience higher hemodynamic stresses. *Neurosurgery* 73(3):497–
519 505
- 520 Alnaes MS, Isaksen J, Mardal KA, Morgan BRMK, Ingebrigtsen T (2007) Compu-
521 tation of hemodynamics in the circle of Willis. *Stroke* 38(9):2500–2505
- 522 Antiga L, Steinman DA (2004) Robust and objective decomposition and mapping of
523 bifurcating vessels. *IEEE Transactions on Medical Imaging* 23(6):704–713
- 524 Antiga L, Piccinelli M, Botti LA, Ene-Iordache B, Remuzzi A, Steinman DA (2008)
525 An image-based modeling framework for patient-specific computational hemody-
526 namics. *Medical and Biological Engineering and Computing* 46(11):1097–1112
- 527 Baek H, Jayaraman MV, Karniadakis GE (2009) Wall shear stress and pressure dis-
528 tribution on aneurysms and infundibulae in the posterior communicating artery
529 bifurcation. *Annals of Biomedical Engineering* 37(12):2469–2487
- 530 Baharoglu MI, Lauric A, Wu C, Hippelheuser JE, Malek AM (2014) Deviation from
531 optimal vascular caliber control at middle cerebral artery bifurcations harboring
532 aneurysms. *Journal of Biomechanics* 47(13):3318–3324
- 533 Bogunović H, Pozo JM, Villa-Uriol MC, Majoie CB, van den Berg R, Gratama van
534 Andel HAF, Macho JM, Blasco J, San Román L, Frangi AF (2011) Automated
535 segmentation of cerebral vasculature with aneurysms in 3DRA and TOF-MRA
536 using geodesic active regions: An evaluation study. *Medical Physics* 38(1):210–
537 222
- 538 Brown RD, Wiebers DO, Forbes GS (1990) Unruptured intracranial aneurysms and
539 arteriovenous malformations: Frequency of intracranial hemorrhage and relation-
540 ship of lesions. *Journal of Neurosurgery* 73(6):859–863
- 541 Castro MA, Putman CM, Cebra JR (2011) Computational analysis of anterior com-
542 municating artery aneurysm shear stress before and after aneurysm formation.
543 *Journal of Physics: Conference Series* 332:012,001
- 544 Cebra JR, Castro M, Putman CM, Alperin N (2008) Flow-area relationship in inter-
545 nal carotid and vertebral arteries. *Physiological Measurement* 29(5):585–594
- 546 Chen H, Selimovic A, Thompson H, Chiarini A, Penrose J, Ventikos Y, Watton
547 PN (2013) Investigating the influence of haemodynamic stimuli on intracranial
548 aneurysm inception. *Annals of Biomedical Engineering* 41(7):1492–1504
- 549 Doenitz C, Schebesch KM, Zoepfel R, Brawanski A (2010) A mechanism for
550 the rapid development of intracranial aneurysms: a case study. *Neurosurgery*
551 67(5):1213–1221
- 552 Dolan JM, Kolega J, Meng H (2013) High wall shear stress and spatial gradients
553 in vascular pathology: A review. *Annals of Biomedical Engineering* 41(7):1411–
554 1427
- 555 Feaver RE, Gelfand BD, Blackman BR (2013) Human haemodynamic frequency har-
556 monics regulate the inflammatory phenotype of vascular endothelial cells. *Nature*
557 *Communications* 4:1525
- 558 Ford MD, Alperin N, Lee SH, Holdsworth DW, Steinman DA (2005) Characteriza-
559 tion of volumetric flow rate waveforms in the normal internal carotid and vertebral

- 560 arteries. *Physiological Measurement* 26(4):477–488
- 561 Ford MD, Hoi Y, Piccinelli M, Antiga L, Steinman DA (2009) An objective approach
562 to digital removal of saccular aneurysms: Technique and applications. *The British*
563 *Journal of Radiology* 82(SI-1):S55–S61
- 564 Foutarakis GN, Yonas H, Scialabassi RJ (1999) Saccular aneurysm formation in curved
565 and bifurcating arteries. *American Journal of Neuroradiology* 20(7):1309–1317
- 566 Frösen J (2014) Smooth muscle cells and the formation, degeneration, and rupture
567 of saccular intracranial aneurysm wall: A review of current pathophysiological
568 knowledge. *Translational Stroke Research* 5(3):347–356
- 569 Fung YC (1997) *Biomechanics: Circulation*, 2nd edn. Springer
- 570 Geers AJ, Larrabide I, Radaelli AG, Bogunović H, Kim M, Gratama van Andel HAF,
571 Majoie CB, VanBavel E, Frangi AF (2011) Patient-specific computational hemo-
572 dynamics of intracranial aneurysms from 3D rotational angiography and CT an-
573 giography: An in vivo reproducibility study. *American Journal of Neuroradiology*
574 32(3):581–586
- 575 Geers AJ, Larrabide I, Morales HG, Frangi AF (2014) Approximating hemodynam-
576 ics of cerebral aneurysms with steady flow simulations. *Journal of Biomechanics*
577 47(1):178–185
- 578 Geers AJ, Morales HG, Larrabide I, Butakoff C, Bijlenga P, Frangi AF (2015a)
579 Wall shear stress at the initiation site of cerebral aneurysms: Distribution on flat-
580 tened branches. Figshare URL [http://dx.doi.org/10.6084/m9.figshare.](http://dx.doi.org/10.6084/m9.figshare.1153934)
581 [1153934](http://dx.doi.org/10.6084/m9.figshare.1153934)
- 582 Geers AJ, Morales HG, Larrabide I, Butakoff C, Villa-Uriol MC, Engelbrecht G,
583 Bijlenga P, Frangi AF (2015b) Wall shear stress at the initiation site of cerebral
584 aneurysms: Vascular models. Figshare URL [http://dx.doi.org/10.6084/m9.](http://dx.doi.org/10.6084/m9.figshare.1159108)
585 [figshare.1159108](http://dx.doi.org/10.6084/m9.figshare.1159108)
- 586 Gonzalez CF, Cho YI, Ortega HV, Moret J (1992) Intracranial aneurysms: Flow
587 analysis of their origin and progression. *American Journal of Neuroradiology*
588 13(1):181–188
- 589 Gosling RG, King DH (1974) Arterial assessment by Doppler-shift ultrasound. *Pro-*
590 *ceedings of the Royal Society of Medicine* 67(6 Pt 1):447–449
- 591 He X, Ku DN (1996) Pulsatile flow in the human left coronary artery bifurcation:
592 Average conditions. *Journal of Biomechanical Engineering* 118(1):74–82
- 593 Helmlinger G, Geiger RV, Schreck S, Nerem RM (1991) Effects of pulsatile flow
594 on cultured vascular endothelial cell morphology. *Journal of Biomechanical Engi-*
595 *neering* 113(2):123–131
- 596 Himburg HA, Dowd SE, Friedman MH (2007) Frequency-dependent response of the
597 vascular endothelium to pulsatile shear stress. *American Journal of Physiology: Heart and Circulatory Physiology* 293(1):H645–H653
- 598 Hop JW, Rinkel GJ, Algra A, van Gijn J (1997) Case-fatality rates and functional
599 outcome after subarachnoid hemorrhage: a systematic review. *Stroke* 28(3):660–
600 664
- 601
- 602 Humphrey JD, Taylor CA (2008) Intracranial and abdominal aortic aneurysms: Sim-
603 ilarities, differences, and need for a new class of computational models. *Annual*
604 *Review of Biomedical Engineering* 10:221–246

- 605 Ingebrigtsen T, Morgan MK, Faulder K, Ingebrigtsen L, Sparr T, Schirmer H (2004)
606 Bifurcation geometry and the presence of cerebral artery aneurysms. *Journal of*
607 *Neurosurgery* 101(1):108–113
- 608 Jamous MA, Nagahiro S, Kitazato KT, Satoh K, Satomi J (2005) Vascular corro-
609 sion casts mirroring early morphological changes that lead to the formation of sac-
610 cular cerebral aneurysm: An experimental study in rats. *Journal of Neurosurgery*
611 102(3):532–535
- 612 Jansen IGH, Schneiders JJ, Potters WV, van Ooij P, van den Berg R, VanBavel E,
613 Marquering HA, Majoie CBLM (2014) Generalized versus patient-specific in-
614 flow boundary conditions in computational fluid dynamics simulations of cere-
615 bral aneurysmal hemodynamics. *American journal of Neuroradiology* 35(8):1543–
616 1548
- 617 Karmonik C, Yen C, Diaz O, Klucznik R, Grossman RG, Benndorf G (2010) Tempo-
618 ral variations of wall shear stress parameters in intracranial aneurysms-importance
619 of patient-specific inflow waveforms for CFD calculations. *Acta Neurochirurgica*
620 152(8):1391–1398
- 621 Kayembe KN, Sasahara M, Hazama F (1984) Cerebral aneurysms and variations in
622 the Circle of Willis. *Stroke* 15(5):846–850
- 623 Kondo S, Hashimoto N, Kikuchi H, Hazama F, Nagata I, Kataoka H (1997) Cere-
624 bral aneurysms arising at nonbranching sites: An experimental Study. *Stroke*
625 28(2):398–403
- 626 Kono K, Terada T (2013) Hemodynamics of 8 different configurations of stenting for
627 bifurcation aneurysms. *American Journal of Neuroradiology* 34(10):1980–1986
- 628 Kono K, Fujimoto T, Terada T (2014) Proximal stenosis may induce initiation of
629 cerebral aneurysms by increasing wall shear stress and wall shear stress gradient.
630 *International Journal for Numerical Methods in Biomedical Engineering* [Epub
631 ahead of print]
- 632 Ku DN, Giddens DP, Zarins CK, Glagov S (1985) Pulsatile flow and atherosclerosis
633 in the human carotid bifurcation: Positive correlation between plaque location and
634 low oscillating shear stress. *Arteriosclerosis* 5(3):293–302
- 635 Kulcsar Z, Ugron A, Marosfoi M, Berentei Z, Paál G, Szikora I (2011) Hemodynam-
636 ics of cerebral aneurysm initiation: The role of wall shear stress and spatial wall
637 shear stress gradient. *American Journal of Neuroradiology* 32(3):587–594
- 638 Lauric A, Hippelheuser J, Safain MG, Malek AM (2014) Curvature effect on hemo-
639 dynamic Conditions at the inner bend of the carotid siphon and its relation to
640 aneurysm formation. *Journal of Biomechanics* [Epub ahead of print]
- 641 Lee SW, Antiga L, Steinman DA (2009) Correlations among indicators of disturbed
642 flow at the normal carotid bifurcation. *Journal of Biomechanical Engineering*
643 131(6):061,013
- 644 Mantha AR, Karmonik C, Benndorf G, Strother C, Metcalfe RW (2006) Hemo-
645 dynamics in a cerebral artery before and after the formation of an aneurysm. *Ameri-
646 can Journal of Neuroradiology* 27(5):1113–1118
- 647 Markl M, Frydrychowicz A, Kozerke S, Hope M, Wieben O (2012) 4D flow MRI.
648 *Journal of Magnetic Resonance Imaging* 36(5):1015–1036
- 649 Marzo A, Singh PK, Larrabide I, Radaelli AG, Coley SC, Gwilliam M, Wilkinson
650 I, Lawford PV, Reymond P, Patel U, Frangi AF, Hose DR (2011) Computational

- 651 hemodynamics in cerebral aneurysms: The effects of modeled versus measured
652 boundary conditions. *Annals of Biomedical Engineering* 39(2):884–896
- 653 McGah P, Levitt MR, Barbour MC, Morton RP, Nerva JD, Mourad PD, Ghodke BV,
654 Hallam DK, Sekhar LN, Kim LJ, Aliseda A (2014) Accuracy of computational
655 cerebral aneurysm hemodynamics using patient-specific endovascular measure-
656 ments. *Annals of Biomedical Engineering* 42(3):503–514
- 657 Meng H, Wang Z, Gao BL, Hoi Y, Metaxa EM, Swartz DD, Kolega J (2007) Complex
658 hemodynamics at the apex of an arterial bifurcation induces vascular remodeling
659 resembling cerebral aneurysm initiation. *Stroke* 38(6):1924–1931
- 660 Meng H, Tutino VM, Xiang JP, Siddiqui A (2014) High WSS or low WSS? Com-
661 plex interactions of hemodynamics with intracranial aneurysm initiation, growth,
662 and rupture: Toward a unifying hypothesis. *American Journal of Neuroradiology*
663 35(7):1254–1262
- 664 Metaxa EM, Tremmel M, Natarajan SK, Xiang JP, Paluch RA, Mandelbaum M, Sid-
665 diqui AH, Kolega J, Mocco J, Meng H (2010) Characterization of critical hemo-
666 dynamics contributing to aneurysmal remodeling at the basilar terminus in a rabbit
667 model. *Stroke* 41(8):1774–1782
- 668 Miura Y, Ishida F, Umeda Y, Tanemura H, Suzuki H, Matsushima S, Shimosaka S,
669 Taki W (2013) Low wall shear stress is independently associated with the rupture
670 status of middle cerebral artery aneurysms. *Stroke* 44(2):519–521
- 671 Morales HG, Larrabide I, Geers AJ, Roman LS, Blasco J, Macho JM, Frangi AF
672 (2013) A virtual coiling technique for image-based aneurysm models by dynamic
673 path planning. *IEEE Transactions on Medical Imaging* 32(1):119–129
- 674 Nealen A, Igarashi T, Sorkine O, Alexa M (2006) Laplacian mesh optimization. In:
675 Proceedings of the 4th International Conference on Computer Graphics and Inter-
676 active Techniques in Australasia and Southeast Asia (GRAPHITE), Kuala Lumpur,
677 Malaysia, pp 381–389
- 678 Nixon AM, Gunel M, Sumpio BE (2010) The critical role of hemodynamics in the
679 development of cerebral vascular disease. *Journal of Neurosurgery* 112(6):1240–
680 1253
- 681 Peiffer V, , Sherwin SJ, Weinberg PD (2013a) Computation in the rabbit aorta of
682 a new metric – the transverse wall shear stress – to quantify the multidirectional
683 character of disturbed blood flow. *Journal of Biomechanics* 46(15):2651–2658
- 684 Peiffer V, Sherwin SJ, Weinberg PD (2013b) Does low and oscillatory wall shear
685 stress correlate spatially with early atherosclerosis? A systematic review. *Cardio-
686 vascular Research* 99(2):242–250
- 687 Penn DL, Komotar RJ, Connolly ES (2011) Hemodynamic mechanisms underlying
688 cerebral aneurysm pathogenesis. *Journal of Clinical Neuroscience* 18(11):1435–
689 1438
- 690 Piccinelli M, Veneziani A, D A Steinman DA, Remuzzi A, Antiga L (2009) A
691 framework for geometric analysis of vascular structures: Application to cerebral
692 aneurysms. *IEEE Transactions on Medical Imaging* 28(8):1141–1155
- 693 Piccinelli M, Bacigaluppi S, Boccardi E, Ene-Iordache B, Remuzzi A, Veneziani A,
694 Antiga L (2011) Geometry of the internal carotid artery and recurrent patterns
695 in location, orientation and rupture status of lateral aneurysms: An image-based
696 computational study. *Neurosurgery* 68(5):1270–1285

- 697 Sadasivan C, Fiorella DJ, Woo HH, Lieber BB (2013) Physical factors effecting cere-
698 bral aneurysm pathophysiology. *Annals of Biomedical Engineering* 41(7):1347–
699 1365
- 700 Sforza DM, Tateshima CMPS, nuela FV, Cebal JR (2012) Effects of perianeurysmal
701 environment during the growth of cerebral aneurysms: A case study. *American*
702 *Journal of Neuroradiology* 33(6):1115–1120
- 703 Shimogonya Y, Ishikawa T, Imai Y, Matsuki N, Yamaguchi T (2009) Can temporal
704 fluctuation in spatial wall shear stress gradient initiate a cerebral aneurysm? A pro-
705 posed novel hemodynamic index, the gradient oscillatory number (GON). *Journal*
706 *of Biomechanics* 42(4):550–554
- 707 Singh PK, Marzo A, Howard B, Rüfenacht DA, Bijlenga P, Frangi AF, Lawford PV,
708 Coley SC, Hose DR, Patel UJ (2010) Effects of smoking and hypertension on wall
709 shear stress and oscillatory shear index at the site of intracranial aneurysm forma-
710 tion. *Clinical Neurology and Neurosurgery* 112(4):306–313
- 711 Stehbens WE (1989) Etiology of intracranial berry aneurysms. *Journal of Neuro-*
712 *surgery* 70(6):823–831
- 713 Tremmel M, Xiang JP, Hoi Y, Kolega J, Siddiqui A, Mocco J, Meng H (2010) Map-
714 ping vascular response to in vivo Hemodynamics: Application to increased flow at
715 the basilar terminus. *Biomechanics and Modeling in Mechanobiology* 9(4):421–
716 434
- 717 Turjman AS, Turjman F, Edelman ER (2014) Role of fluid dynamics and inflamma-
718 tion in intracranial aneurysm formation. *Circulation* 129(3):373–382
- 719 Villa-Uriol MC, Berti G, Hose DR, Marzo A, Chiarini A, Penrose J, Pozo JM,
720 Schmidt JG, Singh PK, Lycett R, Larrabide I, Frangi AF (2011) @neurIST com-
721 plex information processing toolchain for the integrated management of cerebral
722 aneurysms. *Interface Focus* 1(3):308–319
- 723 Watton PN, Raberger NB, Holzapfel GA, Ventikos Y (2009) Coupling the hemo-
724 dynamic environment to the evolution of cerebral aneurysms: Computational
725 framework and numerical examples. *Journal of Biomechanical Engineering*
726 131(10):101,003
- 727 Watton PN, Selimovic A, Raberger NB, Huang P, Holzapfel GA, Ventikos Y (2010)
728 Modelling evolution and the evolving mechanical environment of saccular cerebral
729 aneurysms. *Biomechanics and Modeling in Mechanobiology* 10(1):109–132
- 730 White CR, Haidekker M, Bao X, Frangos JA (2001) Temporal gradients in shear,
731 but not spatial gradients, stimulate endothelial cell proliferation. *Circulation*
732 103(20):2508–2513
- 733 White CR, Stevens HY, Haidekker M, Frangos JA (2005) Temporal gradients in
734 shear, but not spatial gradients, stimulate ERK1/2 activation in human endothe-
735 lial cells. *American Journal of Physiology: Heart and Circulatory Physiology*
736 289(6):H2350–H2355
- 737 Xiang JP, Natarajan SK, Tremmel M, Ma D, Mocco J, Hopkins LN, Siddiqui AH,
738 Levy EI, Meng H (2011) Hemodynamic-morphologic discriminants for intracra-
739 nial aneurysm rupture. *Stroke* 42(1):144–152
- 740 Zhao M, Amin-Hanjani S, Ruland S, Curcio AP, Ostergren L, Charbel FT (2007) Re-
741 gional cerebral blood flow using quantitative MR angiography. *American Journal*
742 *of Neuroradiology* 28(8):1470–1473



Fig. 1 Vascular models of cases with aneurysm (top), cases with the aneurysm virtually removed (middle), and controls (bottom). The ACA is colored red. View points were selected to best visualize the vascular model, so images are not necessarily at the same scale.

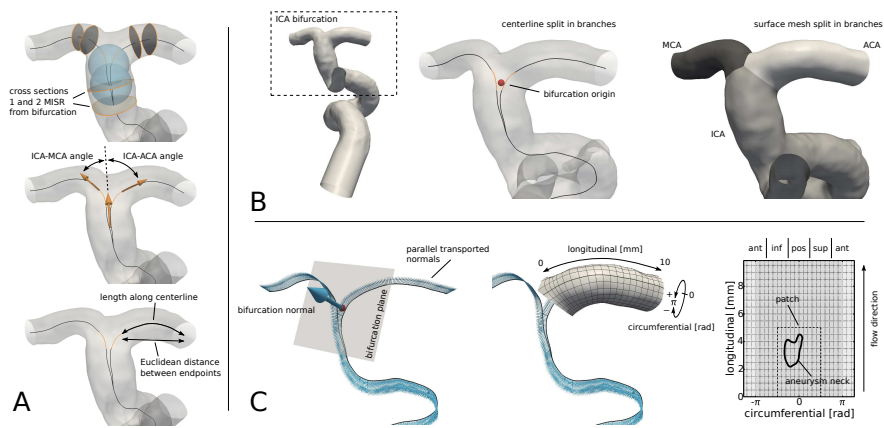


Fig. 2 Post-processing steps. A. Bifurcation sections were created one and two maximally inscribed sphere radii (MISR) away from the bifurcation to obtain representative cross sectional areas for the ICA, ACA and MCA. Bifurcation vectors projected onto the bifurcation plane (panel C) were used to calculate the bifurcation angles. The tortuosity was defined by Eq. (7) using the branch length along the centerline and the Euclidean distance between its endpoints. B. Centerlines from inlet to ACA outlet and inlet to MCA outlet diverged at the ICA bifurcation and were split into branches. Correspondingly, the vessel wall surface was also split into branches. C. The posteriorly directed normal to the bifurcation plane was parallel transported along the centerline. The ACA was mapped onto a 2D parametric space with a longitudinal and a circumferential coordinate. To view the distribution of hemodynamic variables on the whole branch at once, it was flattened onto a rectangle. Plots of the flattened branch indicate the location of the aneurysm neck and the patch. They also indicate the location of the posterior (pos), anterior (ant), superior (sup) and inferior (inf) sides of the branch. The plot range of the circumferential coordinate was slightly extended to show the continuity of the variable distribution. Duplicated regions were grayed out.

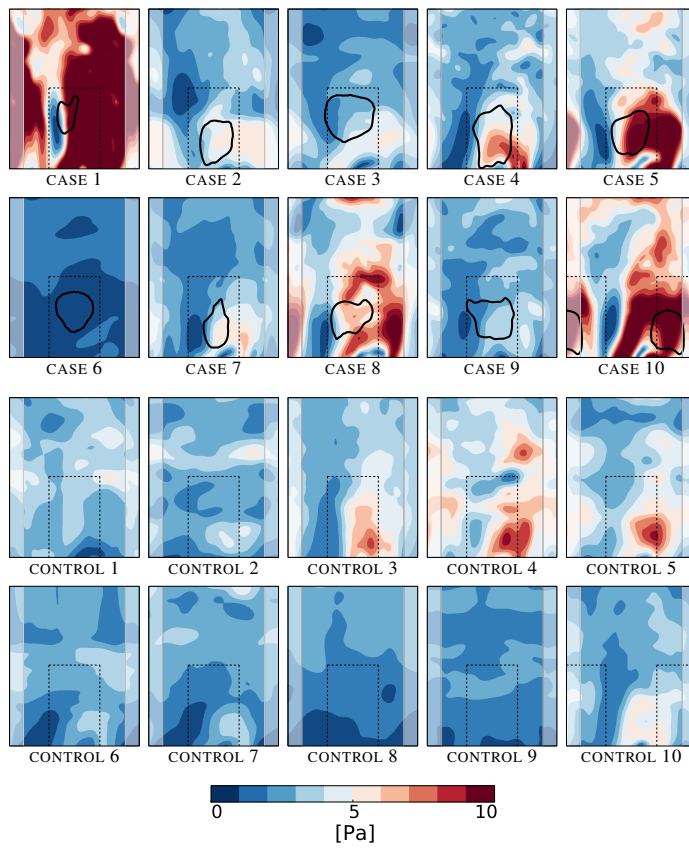


Fig. 3 Time-averaged WSS (TAWSS) under 'normal' inflow conditions. The same colormap range was used for all cases and controls. Plot properties are explained in Figure 2C.

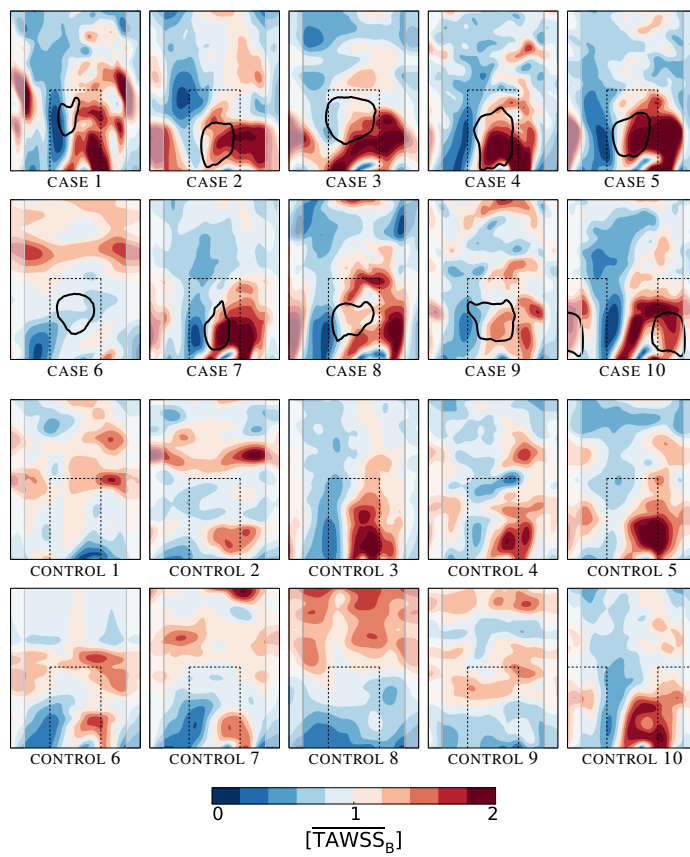


Fig. 4 Time-averaged WSS (TAWSS) under 'normal' inflow conditions. Colormaps were normalized by using $\overline{\text{TAWSS}}_B$ as unit. Plot properties are explained in Figure 2C.

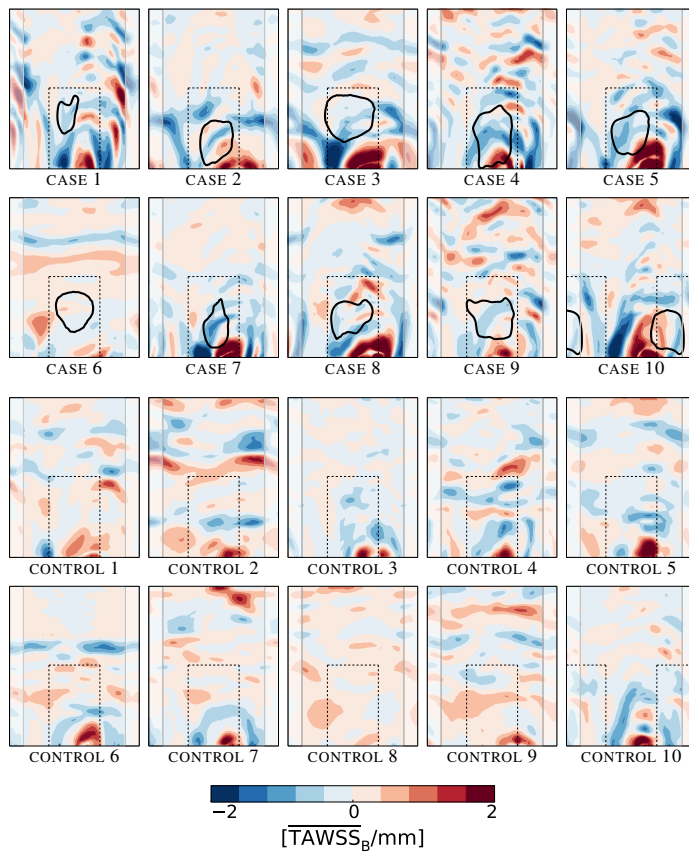


Fig. 5 Gradient of the time-averaged WSS (TAWSSG) under 'normal' inflow conditions. Colormaps were normalized by using $\overline{\text{TAWSS}}_B/\text{mm}$ as unit. Plot properties are explained in Figure 2C.

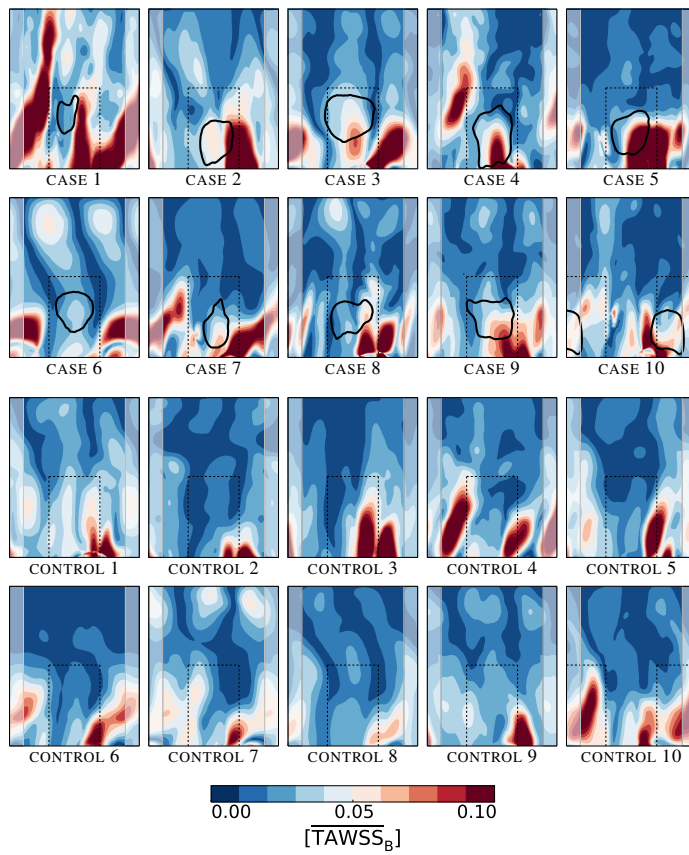


Fig. 6 Transverse WSS (transWSS) under 'normal' inflow conditions. Colormaps were normalized by using $\overline{\text{TAWSS}}_B$ as unit. Plot properties are explained in Figure 2C.

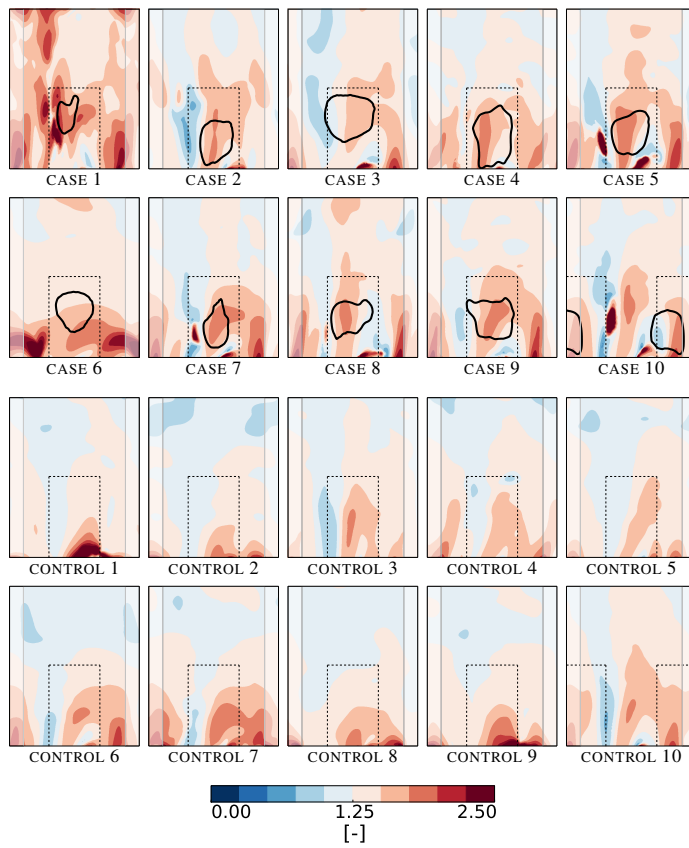


Fig. 7 WSS pulsatility index under 'normal' inflow conditions. The same colormap range was used for all cases and controls. Plot properties are explained in Figure 2C.

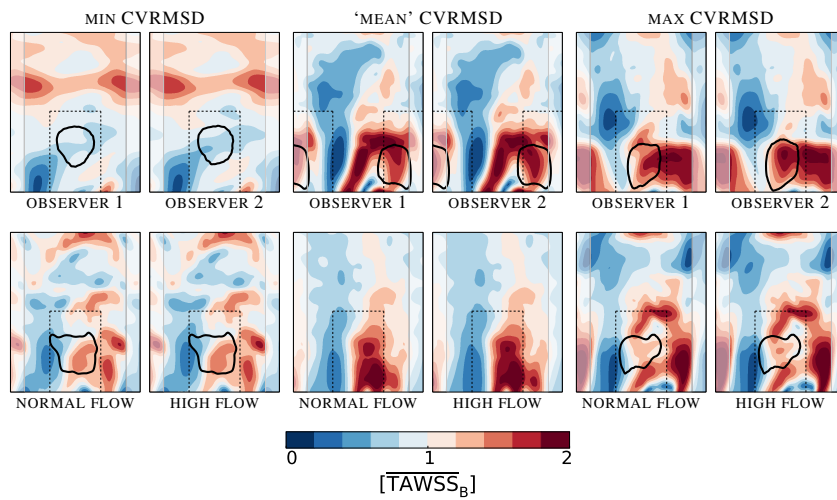


Fig. 8 Comparison of TAWSS distributions between observers removing the aneurysm and between 'normal' and 'high' flow rates at the inlet. Displayed are three cases or controls representing minimum, closest-to-mean and maximum CVRMSD. Colormaps were normalized by using $\overline{\text{TAWSS}}_B$ as unit. Plot properties are explained in Figure 2C.

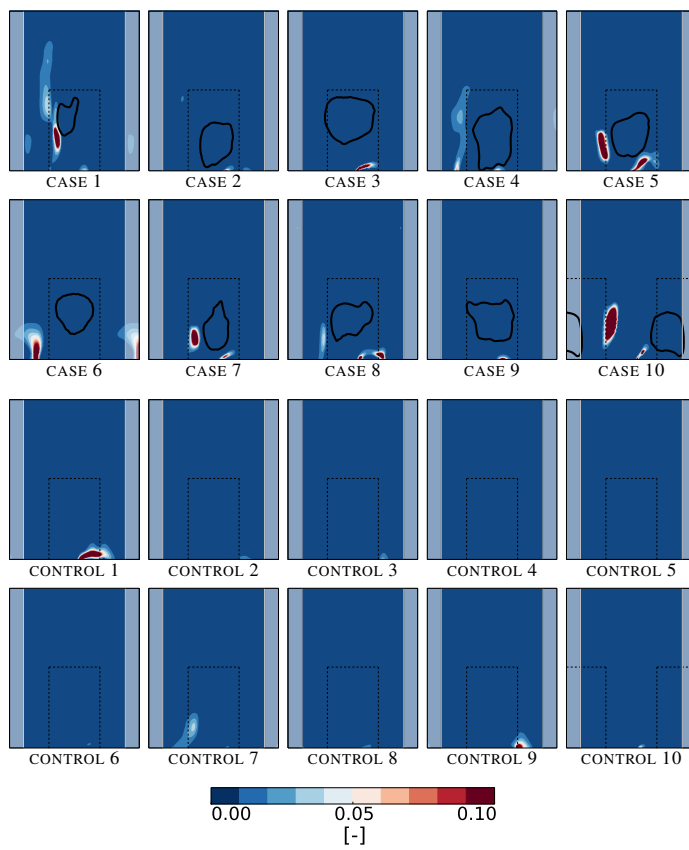


Fig. 9 Oscillatory shear index (OSI). Plot properties are explained in Figure 2C.

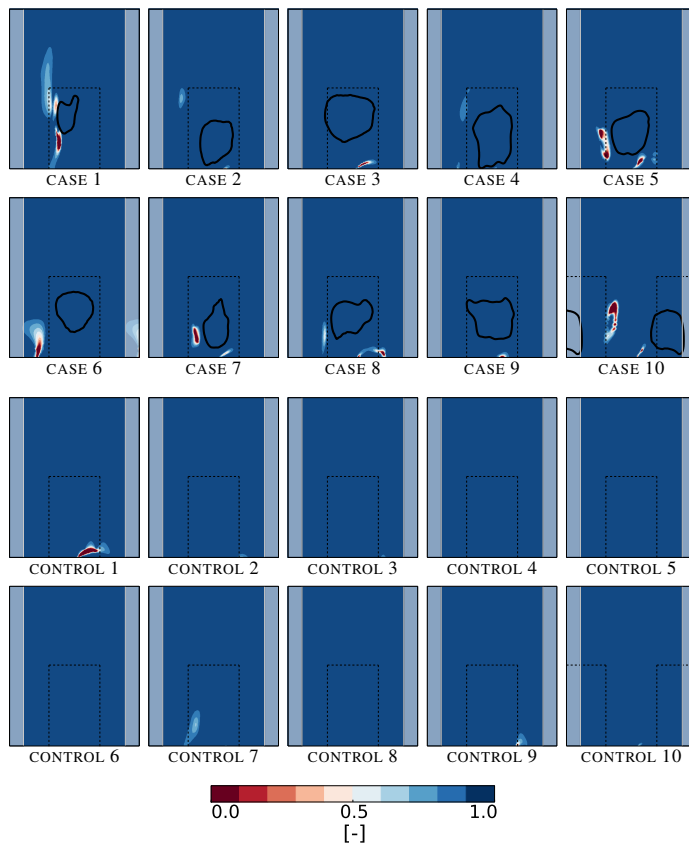


Fig. 10 Aneurysm formation indicator (AFI). Plot properties are explained in Figure 2C.

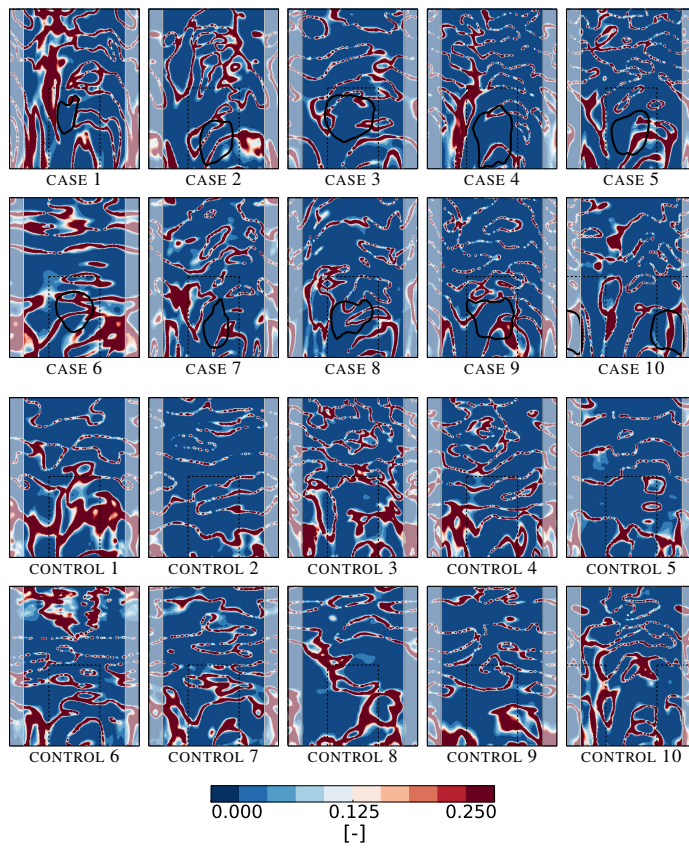


Fig. 11 Gradient oscillatory number (GON). Plot properties are explained in Figure 2C.

Table 1 Statistical analysis of geometric variables.

Variable	Unit	Mean and standard error		<i>p</i> -value ^a
		Cases	Controls	
ICA-ACA angle	[°]	77.8 ± 2.7	77.8 ± 3.1	.880
ICA-MCA angle	[°]	40.3 ± 2.5	39.4 ± 3.0	.940
ICA cross sectional area	[mm ²]	10.7 ± 0.8	9.5 ± 1.0	.364
ACA cross sectional area	[mm ²]	5.2 ± 0.6	3.8 ± 0.3	.059
MCA cross sectional area	[mm ²]	6.0 ± 0.3	5.1 ± 0.3	.049
ICA bifurcation area ratio	[-]	1.05 ± 0.05	0.98 ± 0.05	.545
ACA tortuosity	[-]	0.12 ± 0.03	0.06 ± 0.01	.059

^a *p*-values were calculated with the Wilcoxon rank-sum test; values highlighted in bold face correspond to statistically significant differences with *p* < 0.05.

Table 2 Statistical analysis of hemodynamic variables.

Variable	Unit	Mean and standard error of space-averaged variable values						<i>p</i> -value ^b			
		Cases			Controls			I	II	III	IV
		Patch	Non-patch	Branch	Patch	Non-patch	Branch				
TAWSS	[TAWSS _B]	1.18±0.05	0.94±0.02	1.00±0.00	1.01±0.05	1.00±0.02	1.00±0.00	.022	.959	.034	1.00
TAWSSG ^a	[TAWSS _B /mm]	0.53±0.05	0.34±0.02	0.39±0.02	0.35±0.03	0.26±0.02	0.28±0.02	.017	.013	.010	.003
transWSS	[10 ⁻³ TAWSS _B]	42.7±3.9	26.1±3.0	30.4±2.7	31.4±3.2	21.4±1.1	23.7±1.3	.007	.005	.059	.028
WSSPI	[-]	1.52±0.03	1.38±0.03	1.41±0.03	1.45±0.02	1.27±0.02	1.32±0.02	.005	.005	.082	.003

^a TAWSSG differentiates between positive and negative gradients, so we space-averaged the absolute TAWSSG.

^b *p*-values were calculated with the Wilcoxon rank-sum test; the following samples were compared: I. patch vs. non-patch for the cases (paired), II. patch vs. non-patch for the controls (paired), III. patches of the cases vs. patches of the controls (unpaired), and IV. branches of the cases vs. branches of the controls (unpaired); values highlighted in bold face correspond to statistically significant differences with $p < 0.05$.